# Mapping Coastal Erosion of a Mediterranean Cliff with a Boat-Borne Laser Scanner: Performance, Processing, and Cliff Erosion Rate

Jérémy Giuliano, Thomas Dewez, Thomas Lebourg, Vincent Godard, Mélody Prémaillon, Nathalie Marcot

# Mapping coastal erosion of a Mediterranean cliff with a boat-borne laser scanner: performance, processing and cliff erosion rate

Jérémy Giuliano[abd], Thomas J. B. Dewez[c], Thomas Lebourg[b], Vincent Godard[d], Mélody Prémaillon[c], Nathalie Marçot[c]

[a] *GeoConseil, Risk and Geological Consulting, Le Val 83143, France.*

[b] Université de Nice Sophia Antipolis, CNRS, GéoAzur UMR 7329, Observatoire de la Côte d'Azur, Valbone 06560, France.

[c] Risk and Prevention Direction BRGM, Orléans 45060 and PACA Territorial Direction, Marseille 13009, France.

[d] Aix-Marseille Université, CNRS CEREGE UMR 7330, Aix-en-Provence 13545, France ;

jerem.giuliano@gmail.fr
lebourg@geoazur.unice.fr

t.dewez@brgm.fr
n.marcot@brgm.fr

godard@cerege.fr

---

## Essential title page information

***Corresponding author:***

Thomas DEWEZ

t.dewez@brgm.fr
BRGM Direction des Risques et Prévention,
3 avenue Claude Guillemin
45060 Orléans la Source

***Manuscript information:***

| | *Number* |
|---|---|
| Figure in text | 12 |
| Table in text | 02 |
| | |
| Figure in appendix A | 01 |
| Table in appendix A | 00 |

*Row in the article*
*Start: 1*
*End: 938*
*Total: 938*

### *Abbreviations*

**B**oat**m**ap **s**ystem ® (BMS)

**D**igital Elevation Model **o**f **d**ifference (DoD)

**D**igital **S**urface **M**odel of **e**rosion (DSMe)

**D**rive**m**ap **s**ystem ® (DMS)

**G**eographic **I**nformation **S**ystem (GIS)

**G**lobal **N**avigation **S**atellite **S**ystem (GNSS)

**G**round **S**ampling **D**istance (GSD)

**I**nertial **M**easurement **U**nit (IMU)

**I**terative **C**loset **P**oint (ICP)

**T**errestrial **L**aser **S**canning (TLS)

***Abstract:***

Terrestrial laser scanners (TLS) are well known for providing an efficient means to monitor coastal cliff erosion. Cliffs along micro-tidal coasts, however, have often escaped quantification because the narrow or absent coastal platforms do not offer stable and embracing vantage points. To circumvent this issue, mobile laser scanning surveys from a boat can be used. We present a case study from Provence-Alpes-Côte-d'Azur (Mediterranean coast - southern France) to quantify cliff erosion in such micro-tidal environments. Three surveys were sub-contracted over a period of 17 months to monitor a 3.5-km-long cliff of Carry-le-Rouet (15km west of Marseille). Data quality was check independently using man-made planar walls positioned above the cliff face, to retrieve survey precision and change detection thresholds. Boat-borne mobile lidar system was capable of describing planar features with a precision of 3-4 cm (epoch 1 and 2) and improved to 2.6 cm (epoch 3) with point densities around 100 pts/m². Absolute positioning accuracy varied between 0.1 cm and 0.3 cm. Because the coastline is very sinuous, we describe a method to unfold the point clouds using a continuous analytical surface made of vertical planes joined by arcs of cylinders and perform the analysis in 2.5D. Change was detected using a unique, conservative, threshold of 14 cm (99% quantile estimated on plane change) on grids of 10 x 10 cm pixels. Integrated over the entire cliff face, the average annual cliff recession rate at Carry-le-Rouet is 1.1cm/year. In 17 months, erosion was three times more effective in sandstone and marls layers than in calcarenites and conglomerates. Erosion varies vertically with erosion three times more effective in the lower 25 m of the cliffs than above. Despite imperfections, boat-borne laser scanning system are capable of delivering meaningful erosion data even in this low erosion context.

**Keywords:** Lidar; boat-borne laser scanning; point cloud processing; sea-cliff erosion; Mediterranean coast

---

# 1. INTRODUCTION.

In recent years, a wide range of portable laser scanners has been developed and significant operational improvements make them a choice equipment for field measurements

(Lichti et al., 2000a; Lichti et al., 2000b; Ingensand et al., 2003; Girardeau-Montaut 2005; Heritage and Hetherington, 2007). Among the main geomorphological applications, the study of gravitational processes such as rock falls or landslides (Kemeny and Post, 2003; Bitelli et al., 2004; Teza et al., 2007; Dunning et al., 2009; Dewez et al., 2007; Abellán et al., 2010; Dewez et al., 2013), and evaluation of associated geological hazards (Hunter et al., 2003; Abellán et al., 2006; Jaboyedoff et al., 2009; Furlani et al., 2014) have strongly benefited from these methodological developments. In particular case of inaccessible cliff face, the possibility to monitor spatio-temporal changes of complex surfaces is important for the study of erosion, in order to map the location, dimension and epoch of occurrence of collapse events (Lim et al., 2005 ; Rosser et al., 2005 ; Young and Ashford, 2006 , 2007 ; Dewez et al., 2007 ; Collins and Sitar., 2008 ; Olsen et al., 2009 ; Young et al , 2009 ; Lim et al., 2010 ; Young et al., 2010 ; Dewez et al., 2013; Rohmer and Dewez, 2013; Kuhn and Prüfer, 2014). One of the applications is to interpret the collapse magnitude in terms of erosion activity to appreciate the stage of cliff evolution. For example an increase of rock falls erosion can "pre-date" the occurrence of larger events (Rosser et al., 2007), whereas a decreasing activity may correspond to a temporal "stabilization" (Perdrazzini et al., 2010).

Terrestrial laser scanners (TLS) are particularly suited for the survey of steep cliffs with high resolution and the possibility to deal with complex geometries (Ingensand 2006; Young et al, 2010). Moreover this technique is best adapted to vertical terrain configurations compared to airborne laser scanners. Indeed for aerial technique, high incidence angles between vertical cliff faces and laser beam are responsible for inaccuracy and the lack of vertical measures (Baltsavias, 1999; Young et al., 2010; Earlie et al., 2014). For that reason coastal cliff studies are generally performed with terrestrial laser scanners looking at the cliff face from the beach/platform at the foot of the cliff. This setup requires, however, installing a tripod in front of the cliff, which is not always feasible and especially not along micro-tidal coastline where a dry coastal platform is either narrow or inexistent. We can note also that TLS is not always economical over several kilometer-long sections, because of the effort to assemble all stations together in a rigid reference frame (Michoud et al., 2014).

For these reasons, mobile laser scanning is an attractive technology that allows to scan long-section with high precision (Ellum and El-Sheimy, 2002; Barber et., al, 2008; Jaakkola et al., 2008; Kukko et al., 2012; Glennie et al., 2013). These systems have been adapted on boat configurations in order to detect topographic changes in fluvial environments (Alho et al., 2009; Vaaja et al., 2011, 2013) and more recently in coastal environments (Michoud et al., 2014).

This latter application, over 30-km-long coastal cliffs in northern Europe (Normandy, France), has demonstrated its capability to map geomorphological features smaller than 0.5 $m^2$ (70 x 70cm) and to detect rock fall volume larger than 1 $m^3$ between two acquisitions (in 2012 and 2013).

Here we discuss the example of a 3.5-km-long section of cliff in Provence, along the French Mediterranean coast, near the town of Carry-le-Rouet (15km west of Marseille, *[ Figure 1*). Along this part of the coastline, potential scanning stations are scarce given the micro-tidal regime. Using different mobile mapping systems for time series measurements will become increasingly frequent in the future given the cost, specificity of the equipment, commercial market regulations and rapid technological improvements of mobile mapping equipments. So despite it not being ideal for research purposes, we describe how these different survey data sets were treated and how to assess system performance. Our work is targeted at end-user engineers who are not survey specialists and nevertheless need to independently check the data they paid for.

Repeated surveys were thus performed with a similar mobile boat-borne laser scanner system. In this study we address both generic issues related to the survey technique and allude to site specific information concerning the geomorphic processes at work. First, the positional performance of the different measurement systems and their ability to be combined to produce temporal sequences of point clouds are described: (i) single survey point survey precision; (ii) repeatability of the measures between successive surveys; and (iii) inter-point spacing (i.e. inverse of point density) at each survey epoch. The method employed is particularly adapted in the absence of external model (e.g without terrestrial laser reference). Second, given the sinuous plan-form morphology of the cliff 3D point clouds cannot be readily compared and brought in 2.5D Geographic Information System (GIS) analysis environments for further contextual analyses. We describe a transformation method based on continuous analytical surfaces made of vertical planes and arcs of cylinder to unfold the coastline. The resulting surface is then compatible with cliff face oriented ortho-photography and 2D geological sections drawn in GIS software. Third, this processing workflow is applied to the case study of Carry-le-Rouet where three boat-borne surveys have captured cliff erosion between February 2011 and July 2012. Finally we discuss the boat-borne laser capacity and some first-order geomorphological findings.

## 2. TEST SITE AND STUDY SETTING.

The case study is a section of the Côte-Bleue in Provence region (France), along an East-West 3.5-km-long sea cliff near Carry-le-Rouet town (43°19N, 5°09E). This part of the coast is sinuous and composed of a succession of 5 headlands (*[ Figure 1*-a). Cliff height is comprised between 2 and 56m (relative to the NGF69 terrestrial datum, 1m DEM - Litto3D®V1 IGN-SHOM). The cliff exposes various lithological formations from the Upper Oligocene to Lower Miocene that includes marine marly-sandy-calcareous successions with bed thickness ranging from 0.3 m to 5 m and occasional occurrences of lenticular conglomerates (Demory et al., 2011). The series is made of sub-horizontal to gently South-East dipping beds (2° to 10°) (*[ Figure 1*-b). The cliff profiles present both vertical and inclined faces with well-developed abrasion notches at the foot.

The period of the strongest waves (windstorm from SW and SE) is concentrated in winter, with waves breaking on the coast between 0.5 and more than 2m of height (e.i. Millot, 1990; Ciavola et al., 2007; Sabatier et al., 2019). Rainfall is mainly concentrated in autumn in the form of torrential rain (Lionnello et al., 2006). These rains can correspond to more than 200 mm of water falling only in 24h (Marseille-Marignane weather station, series of 1923-2018).

The rocky shore dynamics along the French Mediterranean cliffs has not been much studied and the respective contributions of marine versus continental contributions in Mediterranean area are not constrained (Furlani et al., 2014). Furthermore, this part of the French coast is not prone to spectacular and/or frequent cliff collapse events, such as those of chalk cliffs of northern Europe (e.g. Duperret et al., 2002; Costa et al. 2004; Regard et al. 2012; Dewez et al., 2013). But risk-wise, the vicinity of the cliff is subjected to an increasing residential, touristic and economic pressures. On the 6$^{th}$ February 2008, a rock fall of about 500 m$^3$ occurred in the central part of our study area (yellow star in *[ Figure 1*-a), precisely in the garden of a villa, leaving less than 2 m between the cliff edge and a swimming pool.

As a consequence, cliff collapse risks have become a major concern for the local populations and authority and cliff collapse hazard quantification was desired in order to characterize the erosion setting. We also need to evaluate if this rock fall corresponds to a rare, isolated, or frequent event. We thus set out to apply the probabilistic analysis framework proposed by Dewez et al (2013) to start assessing cliff collapse hazard.

*[ Figure 1 about here]*

## 3. DATA SETS.

The temporal cliff evolution study in Carry-le-Rouet started with a first survey on 28 February 2011 (epoch 1), with an experimental mobile boat-borne LiDAR mapping system developed by the now-defunct surveying company ATM3D. The following two other surveys, 30 November/1 December 2011 (epoch 2) and 7 July 2012 (epoch 3), were acquired by FUGRO-GEOIDE using two different setups: the Boatmap® system (BMS); and the Drivemap® system (DMS), respectively.

### *3.1. Description of mobile mapping system.*

While each of the three LiDAR mobile mapping systems implemented different hardware specifications (Table 2), the instrumental concept is similar. A rigid frame on the boat contains (*[ Figure 1*-a) a laser scanner, a pair of GNSS antennae and an Inertial Measurement Unit (IMU). The accuracy of the mobile boat positioning system determines the overall performance of the survey.

### *3.2. Point clouds and registration.*

All three point clouds were processed by FUGRO-GEOIDE survey company in Montpellier (France) and delivered as X, Y, Z coordinates expressed in the national Lambert93 reference frame, along with raw LiDAR point intensity value. No other additional data was made available. In total, the complete dataset of all three scans contains 73.2 million points (Table 2). The contractor performed a multi-pass point cloud registration process using both physical targets and point cloud matching with ICP algorithm (e.g. Besl and McKay, 1992). Although locally variable, the quality of multi-pass registration could not be assessed because the point pass identifier (whether west-to-east or east-to-west pass) was not specified in the delivered file, and only a single merged point cloud was delivered to us.

### *3.3. Ortho-photography.*

A series of cliff face photographs were taken in December 2012 and shot with an industrial shutter-free full frame Imperx *16 Mpix* camera fitted with a 50mm lens (Table 2). These photographs were then ortho-rectified by the contractor as a 2-cm-per-pixel continuous

157 ortho-photography. These orthophotos were used for segmenting the point clouds (e.g. on-/off-
158 cliff points and cliff-growing shrubs) and producing litho-stratigraphic sections of cliff rocks (*[*
159 *Figure 1*-b).

*[ Table 1 about here ]*

160

## 161 4. POINT CLOUD: QUALITY ASSESSMENT.

162 Point clouds delivered by subcontractors, or received from an unknown source, often
163 lack a clear description of the data quality. Here we describe an *ad hoc* procedure to retrieve
164 point cloud precision, repeatability, and effective point density empirically. The procedure
165 relies of the fortunate presence of well-distributed man-made walls close to cliff top, which
166 means at a similar distance and incidence to the lidar position as the cliff. Modeled as best-fit
167 planes, these walls serve to empirically derive point precision, accuracy and point density on
168 surface close enough to the cliff, so that statistics from modelling these planes can be
169 extrapolated to the cliff with a reasonable degree of confidence.

170 4.1. Validation metrics and procedure

171 Five walls visible in all three scans. Walls are 4m to 16m in length and 2m to 4m in
172 height. Point cloud precision of a survey corresponds to the amalgamated residuals to the best
173 fit planes (e.g. Monserrat and Croseto, 2008) (*[ Figure 2*-a). Repeatability, or accuracy, assesses
174 whether the successive surveys campaigns located the walls in the same absolute location. It is
175 assessed as the most-likely distance between the best-fit planes of epoch *n* with that of epoch
176 *n+1* (e.g. Besl and McKay, 1992; Michoud et al., 2014) (*[ Figure 2*-b). Because several authors
177 describe errors as not normally distributed (e.g. Höhle & Höhle, 2009, Caudal et al., 2017)
178 classical error propagation cannot be worked out as the sum of residual variances. The threshold
179 value above which cloud-to-cloud differences are not simply due to chance has been worked
180 out in a different fashion. Because the selected walls have remained unchanged between epochs,
181 any cloud to cloud difference observed is noise coming from imprecise measurements. We pick
182 a threshold distance as the empirical quantile at 99.9% (Dewez et al., 2013). Above this value
183 cloud-to-cloud distance has as little as 1 chance in 1000 to be noise.

184 The sum of the squared point precisions and repeatability error gives the shortest
185 distance of the erosion detection, that we call the threshold distance (*[ Figure 2*-c). Finally inter-
186 point spacing (or point density) was also computed to optimize grid pixel sizes required in a

later step and check the delivery for compliance with the survey specifications (e.g. Soudarissanane et al., 2011; Argüelles-Fraga et al., 2013).

To model the planar shape of the walls from XYZ Lambert93 coordinates, a Principal Component Analysis (PCA) was performed. This geometrical transform is preferred to linear regression solution because all X, Y and Z values are known with some degree of error. In this case, the principal component analysis retrieves three components, by decreasing order of variability. The first and second components are wall-coplanar coordinates; the third component is orthogonal to this best-fit plane and describes the dispersion on either sides of the plane (*[ Figure 2*). We should note that wall point cloud samples were segmented well away from the wall edges to avoid contamination by outliers. Unwanted residual distribution deviations could exist if the walls were not true planes. The walls were indeed true planes as residuals plotted versus wall-parallel coordinates did not display coherent high order polynomials trends.

### *4.1. Point precision for single survey (Pp).*

Point to plane distance distribution is often not normally distributed (Höhle & Höhle, 2009). This means that using Gaussian based metrics will not reflect the actual empirical error distribution. To counteract this issue, Höhle & Hohle (2009) used robust quantile-based descriptors, which match empirical distributions. This means describing the central value of a distribution with the median, as opposed to the mean, and describing the dispersion with quantiles of the absolute distance to the median, as opposed to the standard deviation.

Here we use the 99.9% quantile of the absolute deviation to the median as point precision descriptor (Figure 2a, Figure 3). This quality threshold corresponds to a much smaller proportion of points than the usual 5% of a 2-sigma threshold (*[ Figure 2*, Table 3-1) but minimizes the proportion of meaningless differences given the sample size of the millions of points.

### *4.2. Repeatability (R).*

Repeatability describes whether successive surveys position walls in the same location. It was determined by measuring the distance between the point cloud of epoch 2 with modelled planes of epoch 1. The median of this distribution delivers the value of repeatability (Table 3-2).

*[ Figure 2 about here ]*

*[ Figure 3 about here ]*

### *4.3. Threshold distance to detect erosion (Td).*

The remaining cliff pixels exhibit a range of distances that needs thresholding to map eroded blocks. Short distances indicate that the cliff has not changed much while larger values depict erosion more confidently. Picking the appropriate threshold is again a matter of robust statistics. The detection threshold between two point clouds depends on their accuracy, and is obtained by the sum of absolute point precisions and absolute repeatability distances (*[ Figure 2*-c, and Table 3-2).

### *4.4. Inter-point spacing estimation.*

In a later pre-processing stage, the three point clouds are projected into 2.5D grids to enable interactions with ortho-photography and further explore erosion dynamics. The choice of an optimal grid pixel size is a recurrent issue in GIS. Here, we solve it by computing the nearest-neighbour Euclidean distance statistics in wall-coplanar coordinates (*[ Figure 4*). This solution is designed for users with little computing power. An alternative would be to compute the volume density in a large enough neighbourhood (e.g. 0.5 m). This option would have the advantage of accounting for possible point density biases linked with lidar line of sight obliquity. Our option nevertheless is equally valid since cliff face and sampling walls have similar orientations. Any line of sight bias on the wall would affect point density on the cliff in the same manner. Because the inter-point spacing is obviously variable in space, a minimum representative inter-points spacing can be obtained by the median values (as Michoud et al., 2014) which minimize influences of outliers (Höhle and Höhle, 2009).

*[ Table 2 about here ]*

*[ Figure 4 about here ]*

## 5. LiDAR DATA PROCESSING.

The scientific problems we wish to solve concern the total mass balance and discrete block erosion over the entire cliff face. In order to do so, local, point-wise erosion can be assessed with 3D cloud-to-cloud distances (e.g. Lague et al. 2013) but mass balance or scar inventories still requires computing an integrated estimate of erosion, either through meshing or gridding. And further, we would like to explain erosion with various methods readily implemented in 2.5D GIS and currently lacking in full-3D software. The data processing workflow therefore consists in a succession of 4 steps: (i) project 3D point clouds into an analytical 2.5D surface (unfolding); (ii) calculate inter-epoch distances (point clouds comparison); (iii) classify and check for point visibility to assess erosion and (iv) threshold cloud-to-cloud distances to retrieve only meaningful erosion (*[ Figure 5*).

*[ Figure 5 about here ]*

### *5.1. 3D to 2.5D projection method.*

The first step consists in projecting 3D points into an unfolded 2.5D cliff surface. Most terrestrial laser scanning studies in rocky coast environments are performed along straight or semi straight cliffs segments (Lim et al., 2005; Dewez et al., 2007 ; Collins and Sitar, 2008 ; Abellán et al., 2010 ; Lim et al., 2010 ; Young et al., 2010 ; Stock et al., 2011 ; Dewez et al., 2013 ; Kuhn and Prüfer, 2014; Michoud et al., 2014) and all of them admit, sometimes implicitly, that when the cliffs become truly 3D, processing is much more difficult.

Full 3D comparisons, like the M3C2 method of Lague et al. 2013, requires computing local plane normals over a given neighbourhood, but plane normals may misbehave at places with sharp gradients. And the characteristic dimensions of cliff smoothness is spatially variable (see Feldmann et al., 2018). On the other hand, it is well known that planar cliff configurations close to 2D or 2.5 D allow the determination of eroded volume through DoD (Digital Elevation Model of difference, Rosser et al., 2005; Abellán et al., 2010; O'Neal and Pizzuto, 2011). But in 3D complex configurations, DoD will poorly depict strongly oblique surfaces. The coast of Carry-le-Rouet is very sinuous, with a succession of headlands and bays and needs be simplified (*[ Figure 1*-a).

To simplify the visualization and processing of 3D configuration in 2.5D, we detail a method to unfold point clouds (*[ Figure 6*). The numerical method consists in rotated XY coordinates onto a vertical surface made either of contiguous planes sections or arcs of cylinders. Elevation coordinates, Z, remain unchanged. One of two types of transformations are applied: (i) an angular rotation for planar sections (*[ Figure 6*-c1); (ii) and an angular distance calculation for cylindrical sections (*[ Figure 6*-c2).

- For each rectilinear section, unfolded coordinates ($X_U$, $Y_U$) of sub-cloud are obtained by applying a rotation of $-\alpha$ to the initial points (X, Y), which corresponds to the angle between the rectilinear section and the re-projected straight line (*[ Figure 6*-c1).
- For each circular section defined by a circle O, unfolded coordinates $X_U$ and $Y_U$ of sub-cloud are obtained separately (*[ Figure 7*):
    - $X_U$ coordinate corresponds to the angular distance of the points from the initial arc section (*[ Figure 7*-a):

$$Xu = (R \times \Upsilon) \times US\,[2\pi] \qquad (1)$$

with $R$ the radius of the circle O, $\Upsilon$ the angle between starting section and point to project, then $US$ the unfolding sense (by convention $US = 1$ for inland section at sea, and $US = -1$ for bay section).

    - $Y_U$ coordinate corresponds to the distance of the points from the curviline, positive or negative (*[ Figure 7*-b):

$$Yu = (L - R) \times US \qquad (2)$$

with $L$ the distance between the point to unfold (X, Y) and the center of the circle O.

The same transformation scheme was applied to orthorectify photographs shot in November 2011. For complementary information see the appendix A.

*[ Figure 6 about here ]*

*[ Figure 7 about here ]*

### *5.2. Point clouds comparison method.*

After projecting all point clouds into the 2.5D space, the second step is to quantify changes in range due to cliff erosion. Many authors have argued that cloud-to-cloud distance

comparison was possible and desirable (Girardeau-Montault et al., 2005; Lague et al., 2013). Indeed, gridding or meshing prior to computing a difference is amenable to loss of information or ghost volume creation. Hence, we computed a cloud-to-cloud distance between projected point clouds with *Cloud Compare* software before gridding the result.

### *5.3. Points-cloud segmentation and visibility solution.*

Among all the points measured during the survey, many correspond to irrelevant features: vegetation, houses and man-made features, tourists standing in front of the cliff… The third processing step consists in segmenting the point clouds into object classes.

#### *5.3.1. Classification method.*

Based on the American Society for Photogrammetry & Remote Sensing LAS 1.4 labelling standard, a semi-manual classification of different features was performed (

*[ Figure 8* and *[ Figure 9*). We distinguish the cliff (class identifier 2), all types of vegetation (tree, shrub and grass) which are combined into a single unit (class 3), and two newly created classes: external part of the scene (class 64) and cliff foreground (class 65). This latter class will be further processed in a second stage because it is associated with occlusion problems. This classification was performed manually using orthophotos in a GIS. Mapping produced continuous polygons from which the value of the class was transferred to the point clouds.

#### *5.3.2. Visibility solving method (shadow effects).*

Finally, because laser scanners acquire 3D data with a line-of-sight strategy, full-3D objects are likely to contain unseen faces during acquisition. To limit the extent of these shadows, the survey was performed in at least two passes. Shadows are detrimental for our purpose as cloud-to-cloud comparisons can only compute distances between existing points, and hence may locally present large values along the edges of hidden areas, unduly joining background with foreground points. The classical filtering approach for this problem employs the calculation of the depth-maps (or visibility-maps) from a known scanner viewpoint (for more information see Murakami et al., 1999; Vögtle and Steinle., 2004; Vosselman et al., 2004; Giradeau-Montaut et al., 2005). In our case, however, mobile scanner is constantly on the move and tagging a specific position with its corresponding viewpoint is very difficult. Additionally,

the subcontractors did not provide the space/time scanner trajectory. We therefore had to develop a different approach to solve this visibility problem.

*[ Figure 8 about here ]*

*[ Figure 9 about here ]*

Shadows in the cliff plane were computed from a raster mask of point presence (*[ Figure 10*-a). Mask values of each epoch were labeled as a power of 2. So the sum of visibility masks produces a unique identifying code which determines simultaneously when and how many times points were visible (*[ Figure 10*-b). This visibility mask is then combined with the masks of classified objects (cliff, vegetation and foreground) to retain only the topographic changes of cliff portions. Processing quality depends on the choice of pixel size, and this choice is constrained by the representative inter-point spacing discussed above (*cf. 3.4*).

### *5.4. Threshold volume and erosion estimation.*

Finally, the remaining cliff pixels exhibit a range of distances that needs thresholding to map eroded blocks. The minimum volume of erosion detected is thus the result of the combination between the threshold distance and the surface area of one pixel size (*cf. 3.3* and *3.4*, respectively).

In order to quantify the erosion volume and study rockfall scars properties, we need to estimate the eroded surface area. As such, surface area and volume of estimation eroded material is not possible with cloud-to-cloud comparisons. Some degree of integration is necessary. Cloud to cloud distances of unfolded point clouds are gridded into a 2.5D, 10cm x 10cm, Digital Surface Model of erosion (DSMe, *[ Figure 11*). At this stage of the process, DSMe is acceptable because unfolded points clouds are almost planar (Dewez et al., 2013). This threshold is applied to quantify the total eroded volume.

*[ Figure 10 about here]*

# 6. RESULTS.

## *6.1. Quality assessment.*

The point precision is determined as the distribution of the absolute distance between best-fit wall points and their median (*[ Figure 2*-a &

*[ Figure 3*). Distributions of absolute distances to the median are uni-modal and centered around 0.1cm for epochs 1 and 3. Measurements do not seem biased. At epoch 2, however, the distribution is bimodal with the first mode centered around 1.1 cm, indicating an internal multi-pass registration issue (

*[ Figure 3*). Statistical results of the precision are presented in Table 3.1. Classical point measurement precisions as the 95% quantile (2-sigma) are 2.6 cm (epoch 3) and between 3 and 4cm (epoch 1 and epoch 2), whereas the 99.9% quantile are 4.3 cm (epoch 3) and 8.8 cm (epoch 1 and epoch 2).

Looking at the absolute difference to the median between each distributions of distance to wall plan (*[ Figure 2*-b & Table 3-2), the repeatability error of the three epochs comes to 1 mm (between epochs 2 and 3) and presents a shift of 3 mm (between epochs 1 and 2 and epochs 1 and 3).

The inter-point spacing is obviously variable in space. Its distributions turn out to be uni-modal and asymmetric for all three scans (*[ Figure 4*). They all present similar features, but the distribution mode of epoch 3 corresponds to a denser point spacing. The most frequent inter-point spacing is centered around 16 cm (88% quantile), 8 cm (44% quantile) and 4 cm (38% quantile) for the epoch 1, 2 and 3, respectively. The 1-sigma values (68.3% quantile) are 12, 11.5 and 7.1 cm which corresponds to a density of 69, 76, 178 pts/$m^2$ (epoch 1, 2 and 3). A minimum representative inter-points spacing is obtained by the median values. In this case inter-points spacing is 10, 9 and 5 cm corresponding to a density of 100, 123, and 400 pts/$m^2$ (epoch 1, 2 and 3, respectively). For gridding, we choose an intermediate pixel size of 10 cm and adopted a nearest neighbour interpolation method to fill pixels. Pixels without points remained unfilled.

Detection thresholds as the 99.9% cloud-to-cloud distance quantile from reference walls range between 13.1 cm and 18.6 cm (Table 3-2). To apply a consistent detection through time, we thus pick a compromise value of 14 cm as the minimum distance to consider that erosion really occurred between epoch 1 and 3.

Given point cloud characteristics and processing described, the minimum volume potentially detectable is 0.0014 $m^3$ (i.e. 1.4 liters). No smaller volumes can be detected. This is not to say that erosion scars as small make sense from a geomorphological point of view. In fact, the scar inventory completeness was tested with Stepp's (1972, cited and used by Dewez et al., 2013) method. The probability distribution function of scar volume scales as a regular powerlaw between 0.006 $m^3$ and 0.5 $m^3$. Volumes smaller than 0.006 $m^3$ are not completely counted because of measurements and processing limitations. For larger volumes, erosion did not occur in the 17 months time frame (precisely 492 days) between the first and last survey.

### *6.2. Erosion estimation between epoch 1 and 3.*

Erosion scars show up as scattered patches of erosion values (*[ Figure 11*). The minimum volume of erosion detected is 1.4 liters (i.e. one pixel of 100 $cm^2$ with an erosion detection threshold of 14cm). The total surface of cliff exposed is 30,141 $m^2$ where erosion affected 1,107 $m^2$ (only 3.67% of the exposed cliff). To further compute erosion scars properties, the grids were turned into polygon layers with a GIS software. 14,925 distinct scars make up for a total volume of 323.30 $m^3$ . In space, erosion is scattered over the cliff face (*[ Figure 11*). The largest collapses occurred at "Cap de la Vierge" (cape $H_5$ with a total of 150 $m^3$) and involved the basal sandy marl units (*[ Figure 11*-a). Relative to the inventory, a "substantial" collapse (4 $m^3$) also occurred just below the repairs of the largest-known erosion scar at the area near $H_4$ on the "Barqueroute" cliff. Apart from these large events, smaller ones are scattered over the cliff face.

*[ Figure 11 about here]*

## 7. DISCUSSION.

Although mobile laser scanning systems have been used in various other contexts (Alho et al., 2009; Ellum and El-Sheimy, 2002; Barber et., al, 2008; Jaakkola et al., 2008; Kukko et al., 2012; Glennie et al., 2013; Vaaja et al., 2011, 2013), there are very few published studies which used boat-borne mobile laser acquisition to detect coastal cliff erosion along semi-straight cliffs segments (Michoud et al., 2014). Our work completes Michoud et al's (2014) work for two practical and common situations: (i) in the absence of previous and external

validated reference data (e.g. terrestrial laser scanning) and (ii) in a sinuous configuration with a succession of headlands and bays (*[ Figure 1*).

In the absence of validated and robust reference data, modeling point deviation from planar features visible in all scans provides quality assessment in terms of internal consistency (i.e. the ability to accurately represent an object with known geometry, e.g. López et al 2014). From this we learned that:

- Despite being rocked and rolled by sea waves (20-30 cm of amplitude), boat-borne mobile laser systems are capable of describing, in our case, planar features with a point range precision of 4.3 cm (epoch 3) to 8.8cm (epoch 1 and 2) at the 99.9% quantile (Table 3-1) at distances between 50 m to 300 m from the cliff face. The order of magnitude of precision to be expected with these devices come between 1/1000 and 1/7500 of the distance to the cliff.

- Internal mis-registration may exist between successive passes in front of the cliff during the same survey. Here, epoch 2 was affected by a mis-registration reaching about 3cm between passes. Looking at the residuals distribution to a planar feature may help identify and quantify this defect. Obviously such co-registration error strongly limits the performance of the mapping system, in a particular context of low erosion rates. All efforts should thrive to reach the highest precision. Even though laser scanners used at epoch 2 and 3 appear to be of the same ranging precision, the instantaneous orientation solution (from combined IMU/GNSS) was at fault and was not compensated through software post-processing.

- Because a repeatability error - between 1 and 3 mm - could be reached (Table 3-2), global compensation of the entire surveys are achievable with millimeter accuracy. Consequently, the threshold distances are mostly influenced by point precision values (*[ Figure 2*-c). The rather poor erosion detection thresholds, compared to terrestrial laser scanning, comprised between 13.1 and 18.6cm (Table 3-2) are affected by the poor overall precision of the epoch 1, and the internal bias of epoch 2. Nevertheless, this finding is globally in line with the performances described by Michoud et al., (2014).

- One should note that our statistical accuracy assessment criterion, the 99.9% quantile of cloud-to-cloud differences, suggested by Dewez et al., (2013) is more conservative than in many others studies. For example, in the case where the median absolute deviation threshold is used (Michoud et al., 2014), every point contained a large deviation than

the threshold. The erosion may not be always detected as such. We preferred a conservative approach in a context of low erosion.

In a sinuous coastal configuration, point clouds need to be simplified in order to examine the erosion with various methods readily implemented in 2.5D GIS such as the common DoD approach (Digital Elevation Model of difference, as Rosser et al., 2005; Abellán et al., 2010; O'Neal and Pizzuto, 2011). Therefore the key of the data processing workflow (*[ Figure 5*) is the unfolding method (*[ Figure 6* & *[ Figure 7*). We are, of course, aware of the full-3D M3C2 algorithm developed by Lague et al. (2013), implemented in *Cloud Compare* (Girardeau-Montaut et al., 2005), but computing cloud-to-cloud distances is never the end of the geomorphological analysis. Erosion needs to be compared with other sources of information (e.g. lithological maps), manually segmented or integrated over some meshing scheme. For these operations, 2.5D GIS software remain standard tools for many users, and allow for example to classify point clouds with orthophotos. Although manual processing is error prone and time consuming, early tests with *Canupo* (Brodu and Lague, 2012) were not conclusive to segment vegetation of epoch 1 point cloud, possibly due to the high level of noise and comparatively short cliff-dwelling vegetation.

Finally, the goal of this work was to generate a rock fall scar inventory from the Mediterranean coast of France, which had received little attention for cliff retreat so far. This work was prompted by a strong societal demand. The cliff collapse risk there is high, not because of the collapse hazard, but rather for the high-value assets exposed both along the top and foot of the cliff (houses, beaches… see *[ Figure 1*-a). This work initiated a quantitative assessment of collapse hazard. With a volume of erosion detection limit of 1.4 liters (one pixel of 100 $cm^2$ and a threshold erosion of 14 cm), three first-order collapse hazard information were computed: (i) the overall annual cliff recession rate, (ii) the cliff face erosion map, and (iii) vertical and alongshore synthetic erosion profiles:

-The observed average retreat rate equates to 1.1 cm/year (total eroded volume over 17 months divided by the exposed cliff surface area), which is one order of magnitude smaller than in many coastal cliff settings discussed in the literature (see a broad literature compilation in Premaillon et al., 2018). Macrotidal chalk cliffs of the English Channel erode at 10-50cm/year (Costa et al., 2004; Regard et al., 2012; Dewez et al., 2013), mesotidal hard sedimentary cliffs of NE England at 1-5cm/year (Rosser et al. 2013), and mesotidal marly-limestone cliff of Atlantic coast of Portugal erode faster than 10cm/year (Marques et al., 2006). Furthermore,

such centimeter-scale retreat rates are in line with changes we measured between the 1920'ies and 2010 using vertical aerial photography over the entire coastline of Provence-Alpes-Cote d'Azur (Giuliano, 2015). This retreat rate is also compatible with the rare and occasional events collated in the last decade.

- The erosion scar inventory contains 14,925 distinct patches with erosion thicker than 14 cm. The total erosion affected 1,107 m² of the exposed cliff (3.67%) with a low total volume (about 320 $m^3$ in 17 months) in comparison with the Normandy cliff erosion e.g. 100,000 $m^3$ in 12 months observed by Michoud et al. (2014); although this massive short-term volume is affected by a huge coastal landslide in Dieppe. To further explore the relationship between erosion and rock types, we follow a normalization method proposed by Van Westen (1997) and used in De Guidi and Scudero (2013) whereby the relative response of each lithology to erosion can be ranked and quantified. From the observed erosion map, marls and sands are more prone to erosion (60% chances to be eroded) compared to calcarenites and conglomerates (20% each).

- Alongshore (*[ Figure 12*-a), the scar volumes and surfaces are unevenly distributed and no direct response can easily be picked out with respect to relative headland/bay morphology. This lack of fingerprint can be due to the stochastic nature of rock falls and to the short time span of our observations. We do not regard this statement as conclusive and further work elsewhere will investigate this question. Finally, the vertical profile of erosion (*[ Figure 12*-b) shows that erosion is focused in the lower part of the cliff, between 0 and 10 m elevation. The secondary erosion peak between 20 and 25 m elevation is caused by a single rock fall, east of "Cap de la Vierge" (headland $H_5$). Visual examination of scars are compatible with Rosser et al.'s (2013) suggestion that collapses do propagate progressing from a basal notch at sea-level upward. So Carry-le-Rouet cliffs evolve according to common processes but at a rather slow pace over our 17 months survey interval.

*[ Figure 12 about here]*

## 8. CONCLUSION.

This paper describes methods to deal with 3D point clouds acquisition from a boat-borne laser scanner along sinuous cliffs. Man-made wall planes conveniently located along the top of

518 the coastal cliff were fitted with robust planar models to empirically retrieve precision and
519 accuracy of the surveyed point clouds. Although, full-3D change detection is now possible with
520 recently available software, many contextual interpretations still cannot be fully performed with
521 such software. This is why we describe a method to unfold sinuous coastline point clouds onto
522 analytical surfaces made of vertical plane segments and cylinder arcs (unfolding method).
523 Converting 3D to 2.5D leverages the rich GIS tools set for manual mapping, orthophoto
524 interpretation and conventional geomorphological analysis.

525 Applied to Carry-le-Rouet over a time span of 17 months, the average recession rate
526 comes to 1.1cm/year, when retaining only points with significant differences threshold larger
527 than the 99.9% quantile. Such average recession rate lies at the lower end of cliff recession rates
528 studies world-wide. Erosion was three times more effective in sand/marls than in calcarenites
529 or conglomerates and was mostly focused in the lower part of the cliff. The model of cliff
530 instability propagation from its base upward is also observed in Carry-le-Rouet even though
531 further work is needed to describe it in more detail. At this short time span, cliff erosion is thus
532 dominated by marine processes over continental processes.

533

## 534 Aknowledgements.

535 Jérémy Giuliano's PhD project (2011-2015) and Mélody Prémaillon's Master project (2014) were
536 funded by Region PACA in the framework of project Valse (*Vulnérabilité et Adapation pour les Sociétés*
537 *face aux Erosions de falaise côtières en région Provence Alpes Côte d'Azur*). Mobile laser scanning was
538 funded by Region PACA and DREAL-PACA to BRGM. Thomas Dewez was partially funded by
539 BRGM DEV-ESCARP project. The authors thank Julien Lassauque for his R programing contribution.

## 540 Appendix A. Script for unfolding point clouds (R).

541 Point cloud unfolding was coded in R (R Core Team, 2018) through the custom made
542 Unfolding Point Cloud function. This function can treat quickly any cloud in XYZ *ASCII* format. The
543 script requires two inputs: (i) a point cloud to process which contains the information of each sector
544 and (ii) parameters for coastline trends (either planar or curvilinear) (Figure A-1). Angles values are
545 obtained by the complex number method, through Complex package in R (Becker et al. 1988). The
546 output comes in *ASCII* with both initial and unfolded coordinates.

547 *[ Figure A-1 about here]*

548 ##########################################################################################################

```
################################          I-UNFOLDING POINT CLOUD   ###################################
#############################################################################################################
#
### A- Data input ###
# A1- Points cloud (Figure A-1.a.1)
infile.pc <- file.choose()  # open initial points cloud to be unfolded
pcloud <- as.data.frame(scan(file=infile.pc, what=list(x=numeric(),y=numeric(),z=numeric(),
Rr=numeric(),G=numeric(),B=numeric(),i=numeric(), Sect=numeric()), flush=T, skip=1))
#
# A2- Parameters (Figure A-1.a.2)
infile.pm <- file.choose()# open parameters file for unfolding operations (linear and curvilinaer sections)
pmark<-as.data.frame(scan(file=infile.pm,what=list(ID=0, Sect=0,Type="",Ax=0.0, Ay=0.0, Bx=0.0, By=0.0, Ox=0.0,
Oy=0.0, R=0.0, lsect=0.0, lcum=0.0, US=0.0),skip=1))
pcloud$XU<-NA               # to store x unfolded
pcloud$YU<-NA               # to store y unfolded
#
### B- Loop for unfolding  ###
for (j in 1:length(pmark$Sect)){
# B1- Type of section
  type <- as.character(pmark$Type[j])
  #
  # B2- Selection of parameters related to the section (Figure A-1.a.2)
xA <-pmark$Ax[j]          # X coordinate of start of the section
  yA <-pmark$Ay[j]          # y coordinate ...
  xB <-pmark$Bx[j]          # x coordinate of end of the section
  yB <-pmark$By[j]          # y coordinate ...
  lcum <-pmark$lcum[j]      # lcum : cumulated length at the beginning of the section
  lsect <-pmark$lsect[j]    # lsect : section length
  xO <-pmark$Ox[j]          # x coordinate of the center of the circle
  yO <-pmark$Oy[j]          # y coordinate ...
  R  <-pmark$R[j]           # radius of the circle
  US <- pmark$US[j]         # sense for unfolding
#
  # B3- Selection of points belonging to the section
  lgs <- pcloud[which(pcloud$Sect==j),]
  #
# B4- Unfolding
  if (type=="line"){
    lgUnf <- unfol.line(lgs, xA, yA, xB, yB, lcum)
  } else if (type == "curve"){
    lgUnf <- unfol.curve(lgs, xA, yA, xO, yO, R, US, lcum)
  } else {
  }
  #
  # B5- Data storing
  pcloud$XU[which(pcloud$Sect==j)] <- lgUnf$XU
  pcloud$YU[which(pcloud$Sect==j)] <- lgUnf$YU
} #

### C- Data output (Figure A-1.b) ###
#
output.file <- paste(dirname(infile.pc), "/unfolded24.txt", sep="")
write.table(pcloud, output.file, row.names=F)
#
#############################################################################################################
#################################################    II-FUNCTIONS     ######################################
#############################################################################################################
#
unfol.line <- function(lgs, xA, yA, xB, yB, lcum){
  # Translation of origin
  lgUnf <- data.frame(XU=lgs$x - xA, YU=lgs$y - yA)
  # Rotation
  alpha <- Arg(complex(real=(xB-xA), imaginary=(yB-yA)))
  rot <- matrix(c(cos(alpha), sin(alpha), -sin(alpha), cos(alpha)),ncol=2, nrow=2, byrow=T)
  temp <- t(rot %*% t(cbind(lgUnf$XU, lgUnf$YU)))
  # Translation back to lcum
```

```
  lgUnf$XU <- temp[,1] + lcum
  lgUnf$YU <- temp[,2]
  return(lgUnf)
}
#
##END##
#########################################################################################################
```

# References.


Abellán, A., Vilaplana, J.M., Martínez, J., 2006. Application of a long-range terrestrial laser scanner to a detailed rockfall study at Vall de Núria (Eastern Pyrenees, Spain). Engineering Geology 88 (3-4), 136-148.

Abellán, A., Calvet, J., Vilaplana, J.M., Blanchard, J., 2010. Detection and spatial prediction of rockfalls by means of terrestrial laser scanner monitoring. Geomorphology 119, 162-171.

Alho, P., Kukko, A., Hyyppä, H., Kaartinen, H., Hyyppä, J., Jaakkola, A., 2009. Application of boat-based laser scanning for river survey. Earth Surface Processes and Landforms 34, 1831-1838.

Argüelles-Fraga, R., Ordóñez, C., García-Cortés, S., Roca-Pardiñas, J., 2013. Measurement planning for circular cross-section tunnels using terrestrial laser scanning, Automation in Construction 31, 1-9.

Baltsavias, E.P., 1999. Airborne laser scanning: basic relations and formulas. ISPRS Journal of Photogrammetry and Remote Sensing 54, 199-21.

Barber, D., Mills, J., Smith-Voysey, S., 2008. Geometric validation of a ground-based mobile laser scanning system. ISPRS Journal of Photogrammetry and Remote Sensing 63, 128-141.

Becker, R. A., Chambers, J. M., Wilks, A. R., 1988. The New S Language. Wadsworth & Brooks/Cole.

Besl, P. J., McKay, N. D., 1992. A Method for Registration of 3-D Shapes. IEEE Transactions on pattern analysis and machine intelligence 14 (2), 239-256.

Bitelli, G., Dubbini, M., Zanutta, A., 2004. Terrestrial laser scanning and digital photogrammetry techniques to monitor landslide bodies, in: Altan, O. (Eds.), Proceedings of XX ISPRS Congress, Istanbul, Turkey. Commission V, WG V/2, 246-251.

Brodu, M., Lague, D., 2012. 3D terrestrial lidar data classification of complex natural scenes using amulti-scale dimensionality criterion: Application in geomorphology. ISPRS Journal of Photogrammetry & Remote Sensing 68, 121-134.

Collins, B., Sitar, N., 2008. Processes of coastal bluff erosion in weakly lithified sands, Pacifica, California, USA. Geomorphology 97 (3), 483-501.

Costa, S., Delahaye, D., Freiré-Diaz, S., Davidson, R., Di Nocera, L., and Plessis, E., 2004. Quantification of the Normandy and Picardy chalk cliff retreat by photogrammetric analysis, in Mortimore, R. N. and Duperret, A. (Eds.), Coastal Chalk Cliff Instability, Geological Society, London, Engineering Geology. Special Issue 20, 139-148.

De Guidi, G., Scudero, S., 2013. Landslide susceptibility assessment in the Peloritani Mts. (Sicily, Italy) and clues for tectonic control of relief processes. Natural Hazard and Earth System Sciences 13, 949-963.

Demory. F., Conesa, G., Oudet, J., Mansouri, H., Munch, P., Borgomano, J., Thouveny, N., Lamarche, J., Gisquet, F., Marié, L., 2011. Magnetostratigraphy and paleoenvironments, in Shallow-water carbonates: the Oligocene-Miocene sediments in the northern margin of the Liguro-Provençal basin (West Marseille, southeastern France). Bulletin de la Société Géologique de France 182 (1), 37-55.

Dewez, T. J. B., Rohmer, J. and Closset, L., 2007. Laser survey and mechanical modeling of chalky sea cliff collapse in Normandy, France, in: Mc Innes, R., Jakeways, J., Fairbanks, H. and Mathie, E. (Eds.), Proceedings of Landslides and Climate Change, Challenges and Solutions (Isle of Wight, England). 281-288.

Dewez, T. J. B., Rohmer, J., Regard, V., Cnudde, C., 2013. Probabilistic coastal cliff collapse hazard from repeated terrestrial laser surveys: case study from Mesnil Val (Normandy, northern France), in Conley, D., Masselink; G., Russel, P., O'Hare, T. (Eds.), Proceedings 12th International Coastal Symposium (Plymouth, England), Journal of Coastal Research. Special Issue 65, 702-707.

Dunning, S.A., Massey, C.R., Rosser, N.J., 2009. Structural and geomorphological controls on landslides in the Bhutan Himalaya using Terrestrial Laser Scanning. Geomorphology 103, 17-29.

Duperret, A., Genter, A., Mortimore, R. N., Delacourt, B., De Pomerai, M. R., 2002. Coastal rock cliff erosion by collapse at Puys, France: The role of impervious marl seams within chalk of NW Europe. Journal of Coastal Research 18, 52-61.

Earlie, C.S., Masselink, G,, Russell, P.E., Shail, R.K., 2014. Application of airborne LiDAR to investigate rates of recession in rocky coast environments. Journal of Coast Conservation, 15p, DOI 10.1007/s11852-014-0340-1.

Ellum, C., El-Sheimy, N., 2002. Land-based mobile mapping systems. Photogrammetric Engineering and Remote Sensing 68 (1), 13-17.

Furlani, S., Pappalardo, M., Gomez-Pujol, L., Chelli, A., 2014. The rock coast of the Mediterranean and Black Seas. In : Kennedy, D.M., Stephenson, W.J., Naylor, L.A. (Eds), Rock Coast Geomorphology : A Global Synthesis. Geological Society, London Memoirs, 40, 89-123.

Girardeau-Montaut, D., Roux, M., Marc, R., Thibault, G., 2005. Change Detection on Points Cloud Data acquired with a Ground Laser Scanner. International Archives of Photogrammetry, Remote Sensing and Spatial Information Sciences 36 (3), 30-35.

Glennie, C., Brooks, B., Ericksen, T., Hauser, D., Hudnut, K., Foster, J., Avery, J., 2013. Compact multipurpose mobile laser scanning system-initial tests and results. Remote Sensing 5, 521-538.

Heritage, G., Hetherington, D., 2007. Towards a protocol for laser scanning in fluvial geomorphology. Earth Surface Processes and Landforms 32, 66-74.

Höhle, J., Höhle, M., 2009. Accuracy assessment of digital elevation models by means of robust statistical methods. ISPRS Journal of Photogrammetry & Remote Sensing 64, 398-406.

Hunter, G., Pinkerton, H., Airey, R., Calvari, S., 2003. The application of a long-range laser scanner for monitoring volcanic activity on Mount Etna. Journal of Volcanolology and Geothermal Research 123, 203-210.

Ingensand, H., 2006. Metrological Aspects in Terrestrial Laser-Scanning Technology, in: Chrzanowski, A., Wilkins, R. (Eds), Proceedings of 3rd IAG / 12th FIG Symposium, Baden, Germany. 22-24 May.

Ingensand, H., Ryf, A., Schulz, T., 2003. Performances and Experiences in Terrestrial Lasers canning, in: Grün, A., Kahmen, H. (Eds.), Proceedings of Optical 3D-Measurement Techniques VI, Zurich. 22-25 September.

Jaakkola, A., Hyyppä, J., Hyyppä, H., Kukko, A., 2008. Retrieval algorithms for road surface modelling using laser-based mobile mapping. Sensors 8, 5238-5249.

Jaboyedoff, M., Demers, D., Locat, J., Locat, A., Locat, P., Oppikofer, T., Robitaille, D., Turmel, D., 2009. Use of terrestrial laser scanning for the characterization of retrogressive landslides in sensitive clay and rotational landslides in river banks. Canadian Geotechnical Journal 46, 1379-1390.

Kemeny, J., Post, R., 2003. Estimating three-dimensional rock discontinuity orientation from digital images of fracture traces. Computers & Geosciences 29, 65-77.

Kuhn, D., Prüfer, S., 2014. Coastal cliff monitoring and analysis of mass wasting processes with the application of terrestrial laser scanning: A case study of Rügen, Germany. Geomorphology 213, 153-165.

Kukko, A., Kaartinen, H., Hyyppä, J., Chen, Y., 2012. Multiplatform mobile laser scanning: usability and performance. Sensors 12, 11712-11733.

Lague, D., Brodu, N., Leroux, J., 2013. Accurate 3D comparison of complex topography with terrestrial laser scanner: Application to the Rangitikei canyon (N-Z). ISPRS Journal of Photogrammetry & Remote Sensing 82, 10-26.

Lichti, D.D., Steward, M.P., Tsakiri, M., Snow, J., 2000a. Calibration and Testing of a Terrestrial Laser Scanner. International Archives of Photogrammetry, Remote Sensing and Spatial Information Sciences 33 (B5), 485-492.

Lichti, D.D., Steward, M.P., Tsakiri, M., Snow, J., 2000b. Benchmark Tests on a Three-Dimensional Laser Scanning System. Geomatics Research Australia 72, 1-24.

Lim, M., Petley, D. N., Rosser, N. J., Allison, R. J., Long, A. J. and Pybus, D., 2005. Combined digital photogrammetry and time-of-flight laser scanning for monitoring cliff evolution. The Photogrammetric Record 20 (110), 109-129.

Lim, M., Rosser, N. J., Allisson, R. J., Petley, D. N., 2010. Erosional processes in the hard rock coastal cliffs at Staithes, North Yorkshire. Geomorphology 114, 12-21.

López, J., Frances, F., 2010. Influence of the North Atlantic Oscillation and the Western Mediterranean oscillation in the maximum flow events in Spain. International workshop advances in statistical hydrology, may 23-25, 2010 Taormina, Italy.

Marques, F. M. S. F, 2006. Rates, patterns and timing of cliff retreat. A case study on the west of

Portugal. Zeitschrift für Geomorphologie-Supplementbande 144, 231-257.

Michoud, C., Carrea, D., Costa, S., Derron, M.H., Jaboyedoff, M., Delacourt, C., Maquaire, O., Letortu, P., Davidson, R., 2014. Landslide detection and monitoring capability of boat-based mobile laser scanning along Dieppe coastal cliffs, Normandy. Landslides, Technical Note. DOI 10.1007/s10346-014-0542-5.

Monserrat, O., Crosetto, M., 2008. Deformation measurement using terrestrial laser scanning data and least square 3D surface matching. Photogrammetric Engineering and Remote Sensing 63, 142-154.

Murakami, H., Nakagawa, K., Hasegawa, H., Shibata, T and Iwanami, E, 1999. Change detection of buildings using an airborne laser scanner. ISPRS Journal of Photogrammetry & Remote Sensing 54, 148-152.

O'Neal, M.A., Pizzuto, J.E., 2011. The rates and spatial patterns of annual riverbank erosion revealed through terrestrial laser-scanner surveys of the South River, Virginia. Earth Surface Processes and Landforms 36 (5), 695-701.

Olsen, M., Johnstone, E., Driscoll, N., Ashford, S., Kuester, F., 2009. Terrestrial laser scanning of extended cliff sections in dynamic environments: parameter analysis. Journal of Surveying Engineering 135, 161-169.

Pedrazzini, A., Oppikofer, T0, Jaboyedoff, M., Guelli Pons, M., Chantry, R., Stampfli, E., 2010. Assessment of rockslide and rockfall problems in an active quarry: case study of the Arvel quarry (western Switzerland). In: European rock mechanics symposium (EUROCK 2010), Lausanne, Switzerland. CRC Press, Leiden, 593-596.

R Core Team (2018). R: A language and environment for statistical comuting. R Foundation for statistical Computing, Vienna, Austria. ISB 3-900051-07-0, URL http://www.R-project.org

Regard, V., Dewez, T., Bourlès, D.L., Anderson, R.S., Duperret, A., Costa, S., Leanni, L., Lasseur, E., Pedoja, K., Maillet, G.M, 2012. Late Holocene seacliff retreat recorded by 10Be profiles across a coastal platform: Theory and example from the English Channel. Quaternary Geochronology 11, 87-97.

Rohmer, J., Dewez, T.J.B., 2013. On the deviation of extreme sea cliff instabilities from the power law frequency volume distribution: practical implications for coastal management, in Conley, D., Masselink; G., Russel, P., O'Hare, T. (Eds.), Proceedings 12th International Coastal Symposium (Plymouth, England), Journal of Coastal Research. Special Issue 65, 1698-1703.

Rosser, N.J., Brain, M.J., Petley, D.N., Lim, M., Norman, E.C., 2013. Coastline retreat via progressive failure of rocky coastal cliffs. Geology 41, 939-942.

Rosser, N.J, Lim, N., Petley, D.N., Dunning, S., Allison, R.J., 2007. Patterns of precursory rockfall prior to slope failure. Journal of Geophysical Research 112, F04014.

Rosser, N.J., Petley, D.N., Lim, M., Dunning, S.A., Allison, R.J., 2005. Terrestrial laser scanning for monitoring the process of hard rock coastal cliff erosion. Quarterly Journal of Engineering Geology & Hydrgeology 38, 363-375.

Stock, G.M., Bawden, G.W., Green, J.K., Hanson. H., Downing. G., Collins, B.D., Bond, S.D., Leslar, M., 2011. High-resolution three-dimensional imaging and analysis of rock falls in Yosemite Valley, California. Geosphere 7 (2), 573-581.

Schwarz, K.P., Chapman, M.A., Cannon, M.W., Gong, P., 1993. An Integrated INS/GPS Approach to the Georeferencing of Remotely- Sensed Data. Photogrammetric Engineering and Remote Sensing 59 (11), 1667–1674.

Soudarissanane, S., Lindenbergh, R., Menenti, M., Teunissen, P., 2011. Scanning geometry: influencing factor on the quality of terrestrial laser scanning points, ISPRS Journal of Photogrammetry and Remote Sensing. 66, 389-399.

Stock, G.M., Bawden, G.W., Green, J.K., Hanson. H., Downing. G., Collins, B.D., Bond, S.D., Leslar, M., 2011. High-resolution three-dimensional imaging and analysis of rock falls in Yosemite Valley, California. Geosphere 7(2), 573-581.

Stepp's (je ne trouve pas la reference dans l'article Dewez et al., 2013)

Teza, G., Galgaro, A., Zaltron, N., Genevois, R., 2007. Terrestrial laser scanner to detect landslide displacement fields: a new approach. International Journal of Remote Sensing 28, 3425-3446.

Vaaja, M., Hyyppä, J., Kukko, A., Kaartinen, H., Hyyppä, H., Alho, P., 2011. Mapping topography changes and elevation accuracies using a mobile laser scanner. Remote Sensing 3, 587-600.

Vaaja, M., Kukko, A., Kaartinen, H., Kurkela, M., Kasvi, E., Flener, C., Hyyppä, H., Hyyppä, J., Järvelä, J., Alho, P., 2013. Data processing and quality evaluation of a boat-based mobile laser scanning system. Sensors 13, 12497-12515.

Vögtle, T., Steinle, E., 2004. Detection And Recognition of Changes in Building Geometry Derived From Multitemporal Laserscanning Data. International Archives of Photogrammetry, Remote Sensing and Spatial Information Sciences 35 (B2), 428-433.

Vosselman, G., Gorte B.G.H., Sithol, G., 2004. Change Detection for Updating Medium Scale Maps Using Laser Altimetry. International Archives of Photogrammetry, Remote Sensing and Spatial Information Sciences 35 (B3), 207-212.

Young, A.P., Ashford, S.A., 2006. Application of airborne LIDAR for seacliff volumetric change and beach sediment contributions. Journal of Coastal Research 22, 307-318.

Young, A.P., Ashford, S.A., 2007. Quantifying sub-regional seacliff erosion using mobile terrestrial LIDAR. Shore Beach 75, 38-43.

Young, A.P., Flick, R.E., Gutierrez, R., Guza, R.T., 2009. Comparison of short-term seacliff retreat measurement methods in Del Mar, California. Geomorphology 112, 318-323.

Young, A.P., Olsen, M.J., Driscoll, N., Flick, R.E., Gutierrez, R., Guza, R.T., Johnstone, E., Kuester, F., 2010. Comparison of airborne and terrestrial LIDAR estimates of seacliff erosion in southern California. Photogrammetric Engineering & Remote Sensing 76, 421-427.

*Table 1. Technical specifications of the three boat mobile mapping systems (ATM3D, Boat-Map ® and Drive-Map ®).*

| **BOAT MOBILE MAPPING SYSTEM** | | | |
|---|---|---|---|
| **Epoch** | **1 (*February 2011)*** | **2 *(November 2011)*** | **3 *(July 2012)*** |
| **SYSTEM** | **ATM3D** | **BOAT-MAP®** | **DRIVE-MAP ®** |
| **Number of points** | $10.6*10^6$ | $18.7*10^6$ | $43.9*10^6$ |
| ***1. Positionning sensors (GNSS & IMU)*** | | | |
| ***GNSS brand*** | *NOVATEL* | *TRIMBLE* | *TOPCON* |
| **GNSS sampling frequency [Hz]** | 1 | 1 | 20 |
| **Brand (IMU)** | *LandINS (IXSEA)* | *FSAS (NOVATEL)* | *TOPCON* |
| **IMU sampling frequency [Hz]** | 200 | 200 | 100 |
| **Rolling/pitch precision [°]** | 0.005 | 0.008 | 0.02 |
| **Bend precision** | 0.010 | 0.023 | 0.04 |
| ***2. Mapping sensors (LASER scanner)*** | | | |
| **LASER scanner brand** | *LMS Z390i (RIEGL)* | *IIris HD ER (OPTECH)* | *VQ 250 (RIEGL)* |
| **Aperture angle [°]** | 80 | 40 | 360 |
| ***Measurement rate [pts.s$^{-1}$]*** | 11000 | 10000 | 300000 |
| **Distance range [m]** | 1-400 | 3-1800 | 1.5-200 |
| **Angular resolution [°]** | 0.002 | 0.00115 | 0.0018 |
| ***σ angular measured [°]*** | 0.001 | 0.00458 | 0.001 |
| ***σ distance measured [mm]*** | 4 | 7mm-100m | 5 |
| ***3. Camera*** | | | |
| **Camera brand** | - | *Imperx-16M-G(IMPERX)* | - |
| **Focale length [mm]** | - | 35 | - |
| **Sensor length [mm]** | - | 36.07*24.05 | - |
| **Pixel size [Mpx]** | - | 4872*3248 | - |

865

866
867
868
869

871 *Table 2. Synthesis of point clouds quality. 1. Single epoch quality of the three epochs (statistical*
872 *point precision and modal value); 2. Inter epoch quality of the three epochs (point precision,*
873 *repeatability and threshold distance). * The 95 and 68.3 quantiles would be the equivalent of*
874 *classical 2-sigma and 1-sigma thresholds if the distribution were truly Gaussian.*

1. ***Single epoch quality of three point clouds: point precision [cm]***

| ***Epoch*** | | **1 *(February 2011)*** | **2 *(November 2011)*** | **3 *(July 2012)*** |
|---|---|---|---|---|
| ***N walls [pts]*** | | *7630* | *8968* | *23232* |
| **Quantile of absolute distance [cm]** | ***99.9*** | 8.8 | 8.8 | 4.3 |
| | ***95.0 (2σ*)*** | 3.1 | 3.8 | 2.6 |
| | ***68.3 (1σ*)*** | 1.4 | 2.2 | 1.1 |
| | ***50.0*** | 1.0 | 1.6 | 0.7 |
| **Modal value [cm]** | | 0.1 | 1.1 | 0.1 |

2. ***Inter-epoch quality of three point clouds (see [ Figure 2)***

875

| a. Sum of the squared point precision [cm] | | | | + | b. Repeatability distance [cm] | | | | = | c. Threshold distance [cm] | | | |
|---|---|---|---|---|---|---|---|---|---|---|---|---|---|
| | **Epoch 1** | **Epoch 2** | **Epoch 3** | | | **Epoch 1** | **Epoch 2** | **Epoch 3** | | | **Epoch 1** | **Epoch 2** | **Epoch 3** |
| **Epoch 1** | - | - | - | | **Epoch 1** | - | - | - | | **Epoch 1** | - | - | - |
| **Epoch 2** | 17.6 | - | - | | **Epoch 2** | 0.29 | - | - | | **Epoch 2** | 17.9 | - | - |
| **Epoch 3** | 13.1 | 13.1 | - | | **Epoch 3** | 0.31 | 0.13 | - | | **Epoch 3** | 13.4 | 13.2 | - |

876

877

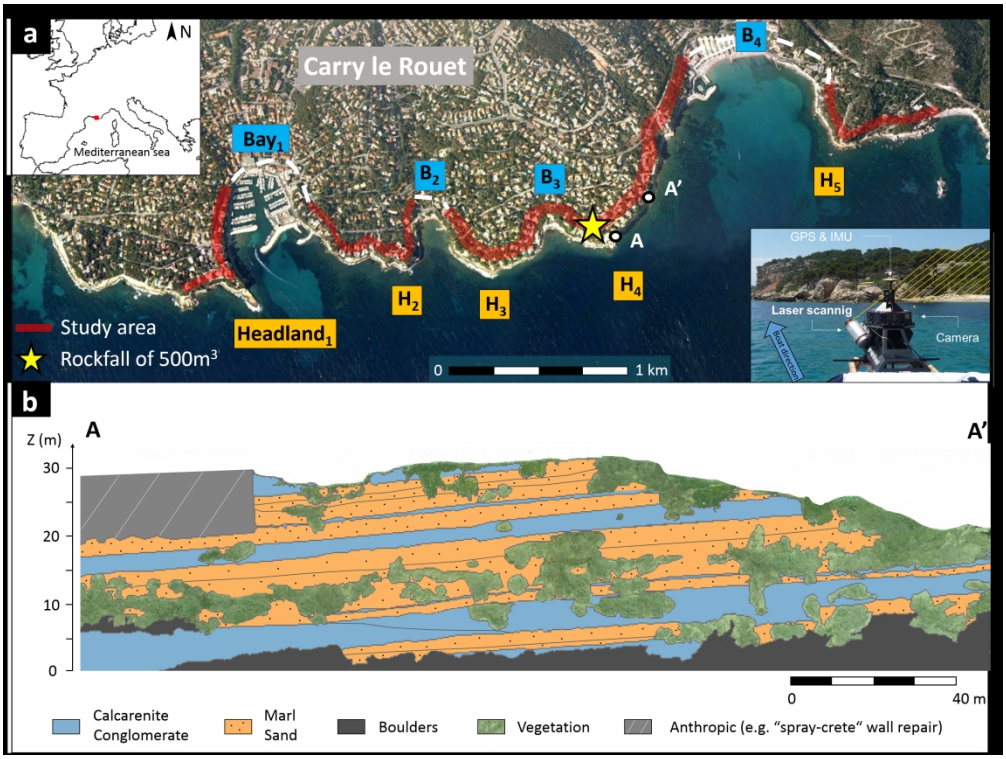


Figure 1. Study site of Carry-le-Rouet along the micro-tidal Mediterranean coastline (15km west of Marseille, southern France). a- Map view of the sinuous coastline composed of 5 headlands and 4 bays and study area; b- Front view of the section AA' and geological interpretation of the Oligo-Miocene sedimentary stack setting drawn from ortho-photography. The "spray-crete" wall repair corresponds to the northern end of a rockfall section of about 500m$^3$ of that occurred on February 6, 2008.

507x380mm (150 x 150 DPI)

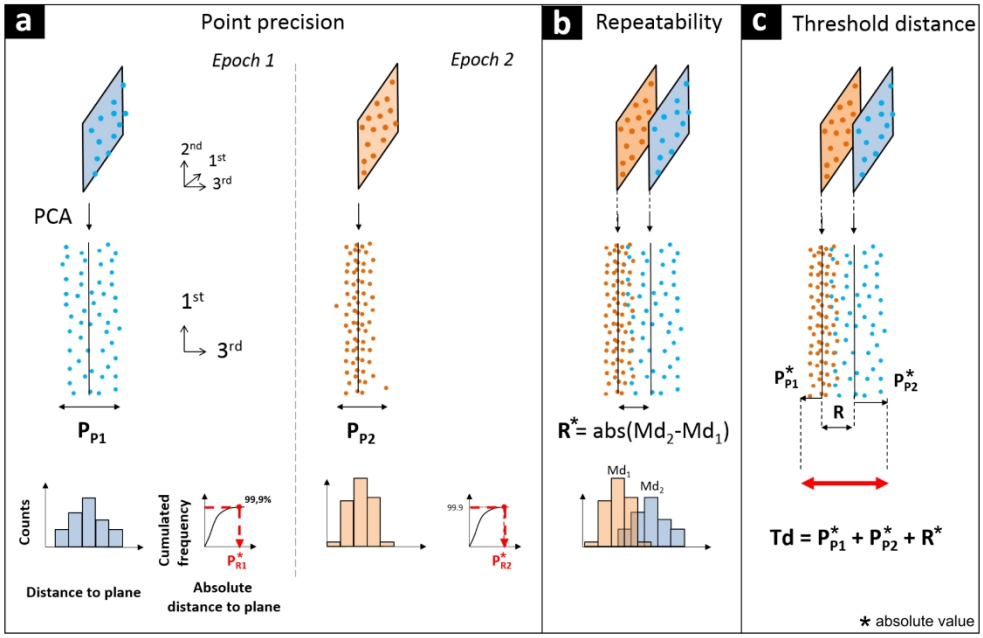


Figure 2. Quality assessment principle applied to a planar object. Point precision (PP), repeatability distance error (R); and threshold distance (Td) assessment through the third component (3rd) of Principal Component Analysis applied to diachronic wall measurements (example for epoch 1 and 2). 3rd component corresponds to distance to wall plan model. a- Point precision (PP1 and PP2) values are obtained as the 99.9% quantile of the cumulated frequency of the absolute 3rd component. b- Repeatability error (R) corresponds to absolute difference of median of the 3rd component values (Md1 and Md2). c- Threshold distance (Td) is the total uncertainty of the detection between two epochs.

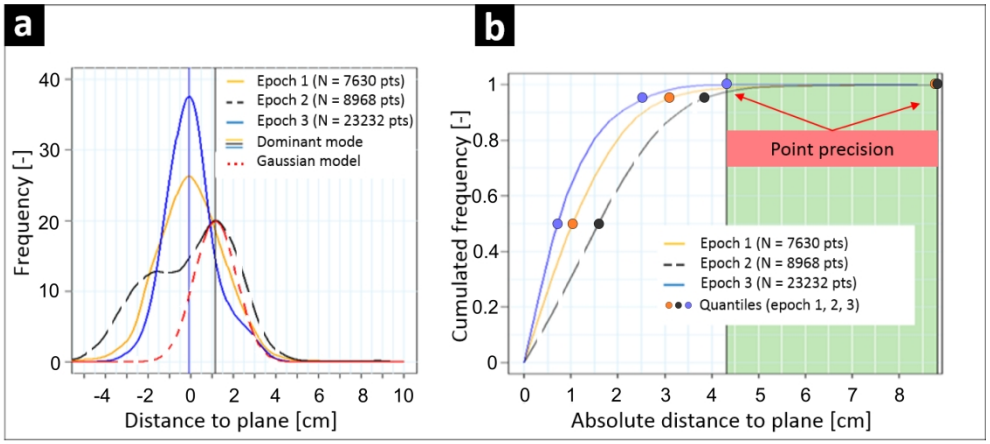


Figure 3. Point precision (PP) assessment. a- Frequency density (bandwidth of 3mm) of PCA third component deviation to the median. Dominant modes (density curve maximum) are marked by vertical lines. The red short-dashed curve represents a Gaussian distribution centered on the dominant mode of the epoch 2. b- Cumulated frequency of absolute deviation from the median. The plain dots represent the 50%, 95% and 99.9% quantiles of each survey. Epoch 2 is more skewed to the right than epochs 1 and 3.

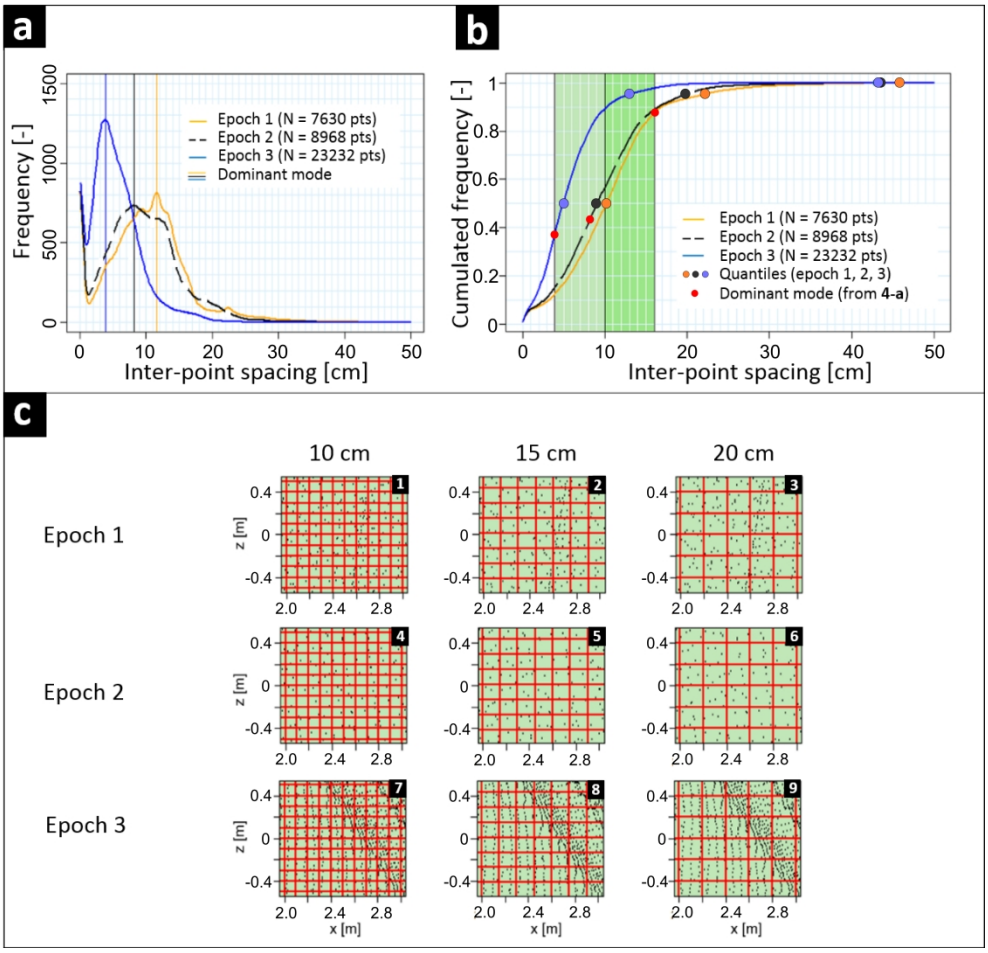


Figure 4. Inter-point assessment determined by a projection of 2.5D grids for the three epochs. a- Frequency density of inter-point Euclidian spacing in a wall-coplanar reference frame (bandwidth = 0.5mm). Dominant modes are defined by vertical lines. b- Cumulated frequency of the inter-point spacing. c- Example of different grid cell size (10, 15, 20cm) applied to point clouds from a wall extracted for the three epochs.

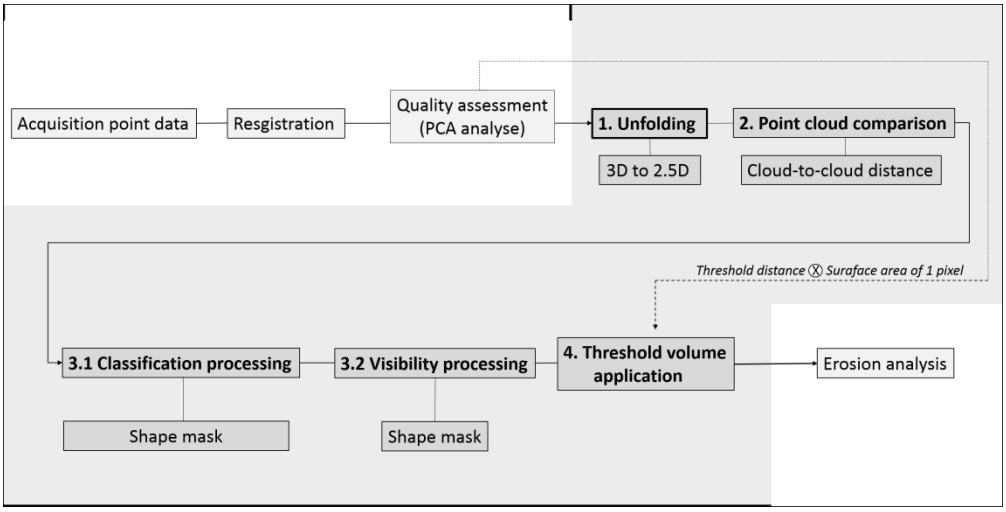


Figure 5. Flow diagram of LiDAR data processing (from data acquisition to erosion analysis). Grey polygon indicates LiDAR data processing based on unfolding method.

438x220mm (150 x 150 DPI)

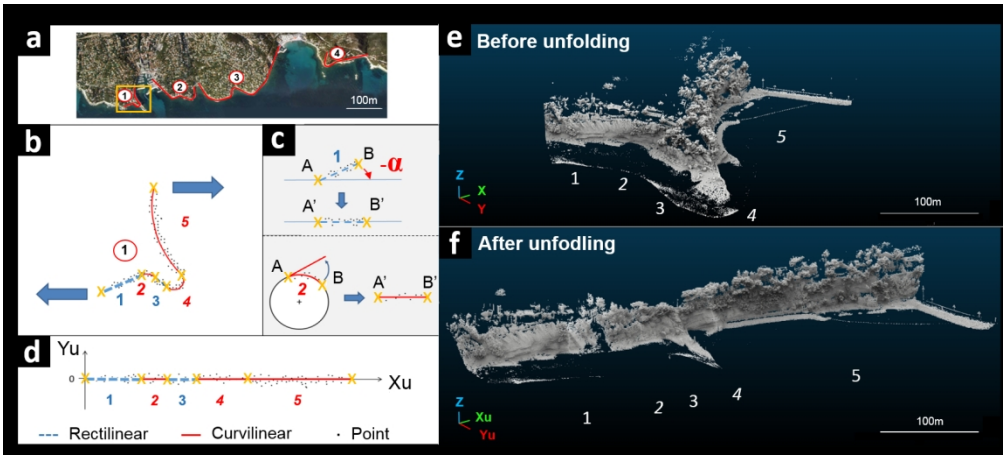


Figure 6. Projection method applied to a complex sinuous point cloud, example of area 1. a- Map view of the general trend of coastline defined through GIS. Map projection is defined in the same system as point clouds. b- Focus of sinuous area 1. General trend and point cloud are segmented into linear (dashed blue line) and curvilinear sections (solid red curve). c. Two types of transformation are applied to sub-point cloud, c.1- angular rotation for rectilinear, and c.2- angular distance calculation for curvilinear section. d. Point cloud unfolded and re-projected in unfolded coordinates along a straight line. e- & f- View of point cloud before and after unfolding.

293x132mm (150 x 150 DPI)

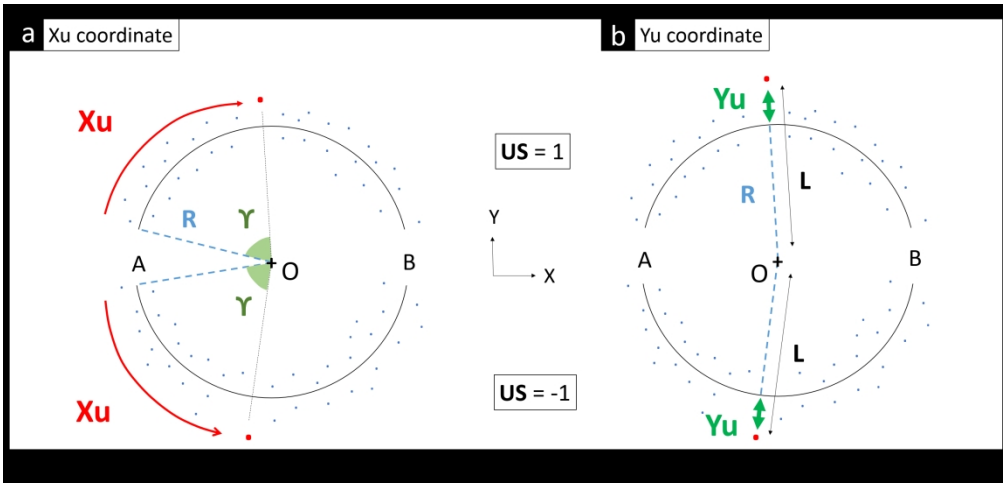


Figure 7. Unfolding method of curvilinear section defined by a circle. Unfolded coordinates XU and YU of sub-clouds are obtained separately. a- XU coordinate corresponds to the angular distance of the points from the initial arc section (A). b- YU coordinate corresponds to the distance of the points from the curvilinear section (AB).

511x245mm (150 x 150 DPI)

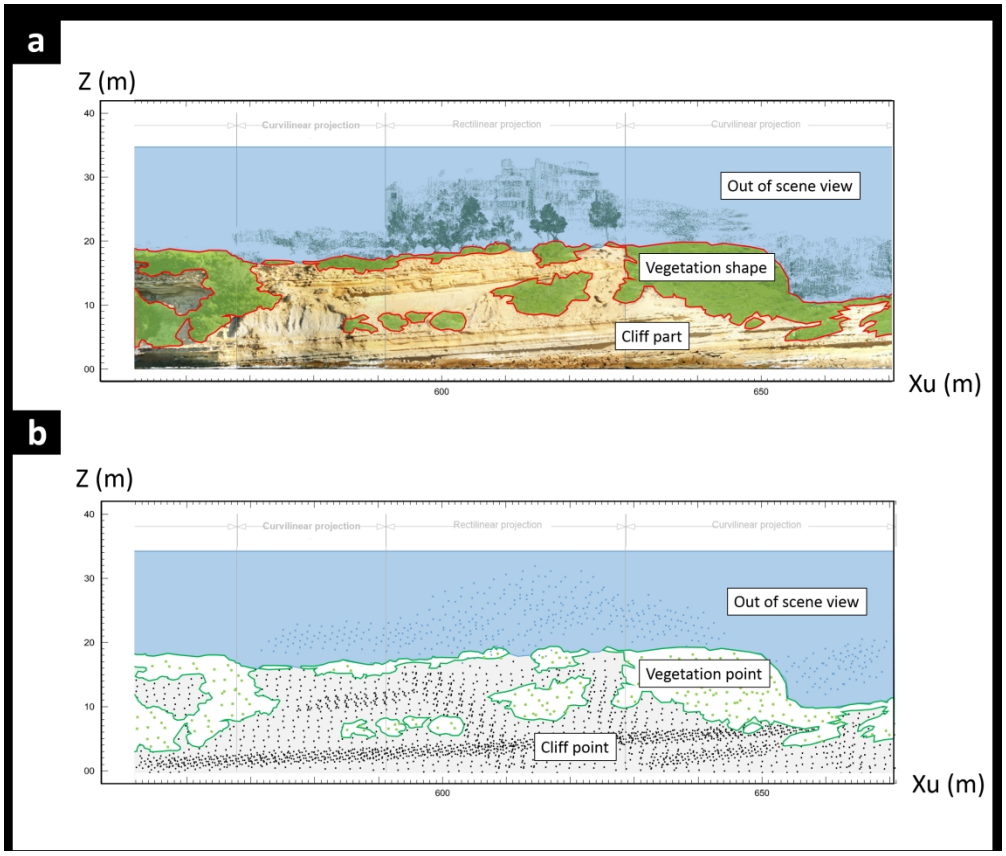


Figure 8. Semi-automatic classification by mask application to an unfolded point cloud. a- Example of a section of an ortho-photography digitalized by three polygons which correspond to "out of scene view", "vegetation" and "cliff". b- Mask segmentation applied by superposition of polygons on the front view (Xu, Z) of unfolded point cloud (in same projection).

408x345mm (150 x 150 DPI)

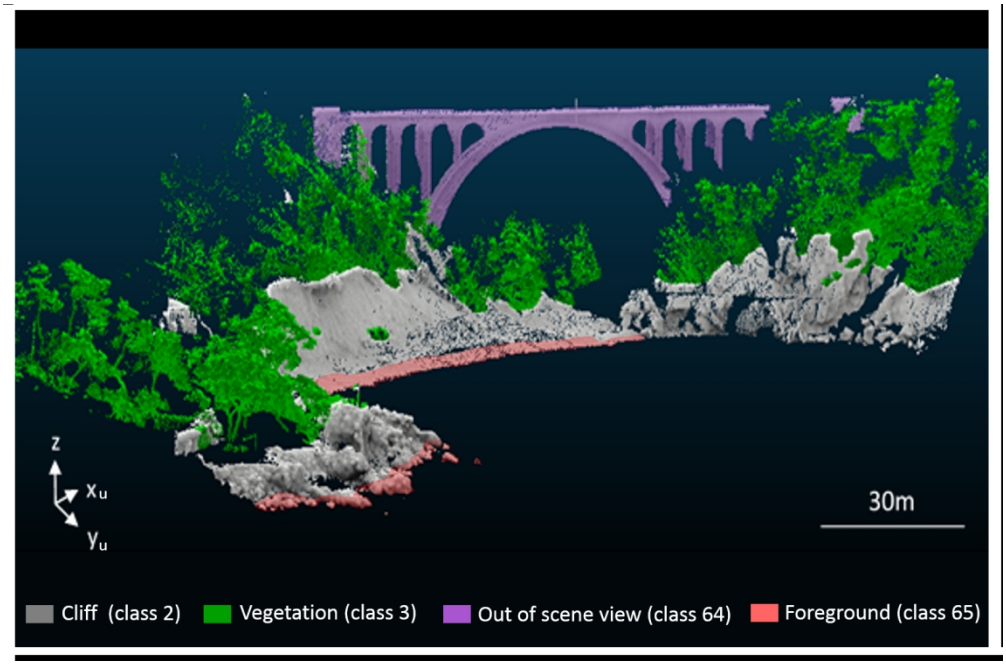


Figure 9. Point cloud processed (unfolded and classified). Example of the eastern section of epoch 3.

281x185mm (150 x 150 DPI)

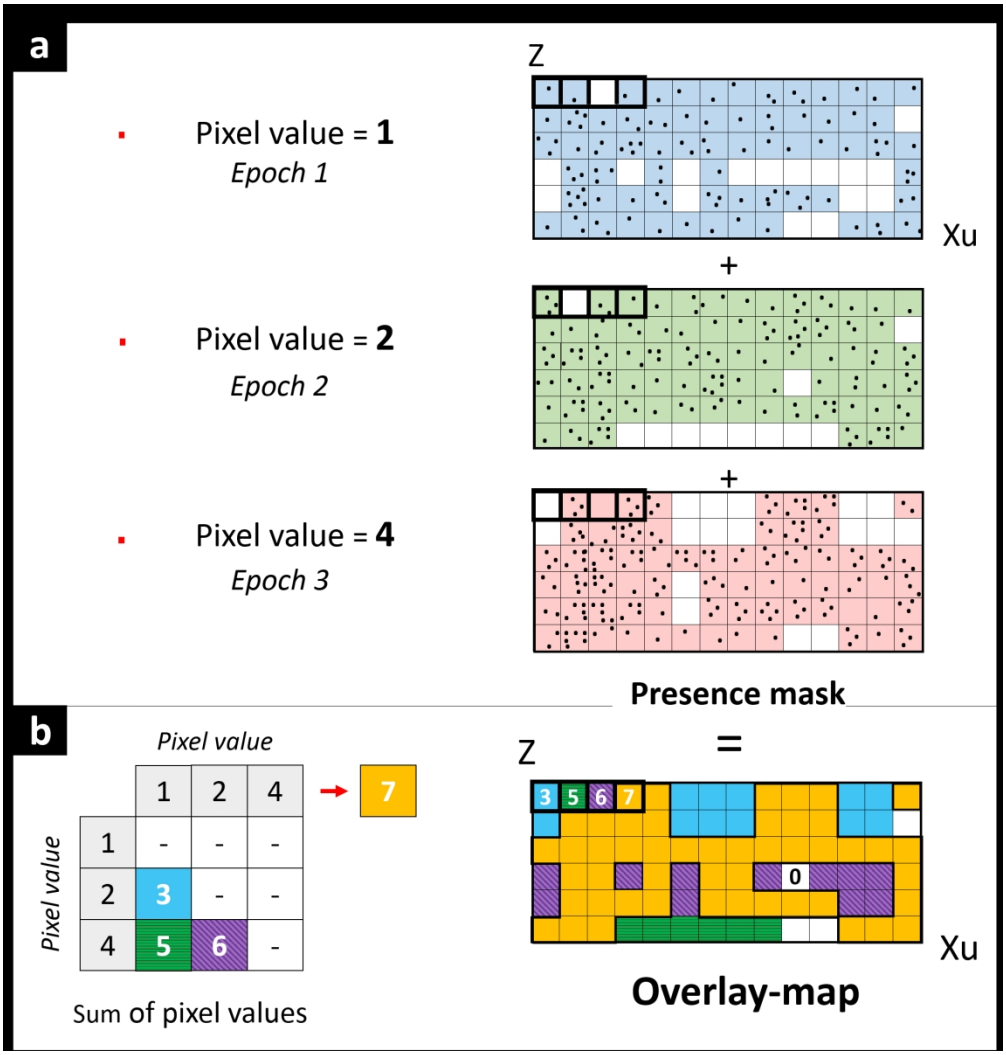


Figure 10. Overlay-map generation in two steps. a- Point presence mask creation for the three epochs. Pixel label is incremented at each epoch. b- Overlay map generated by the sum of the point presence mask. The nominal pixel value shows distinct visibility between the three epochs.

362x378mm (150 x 150 DPI)

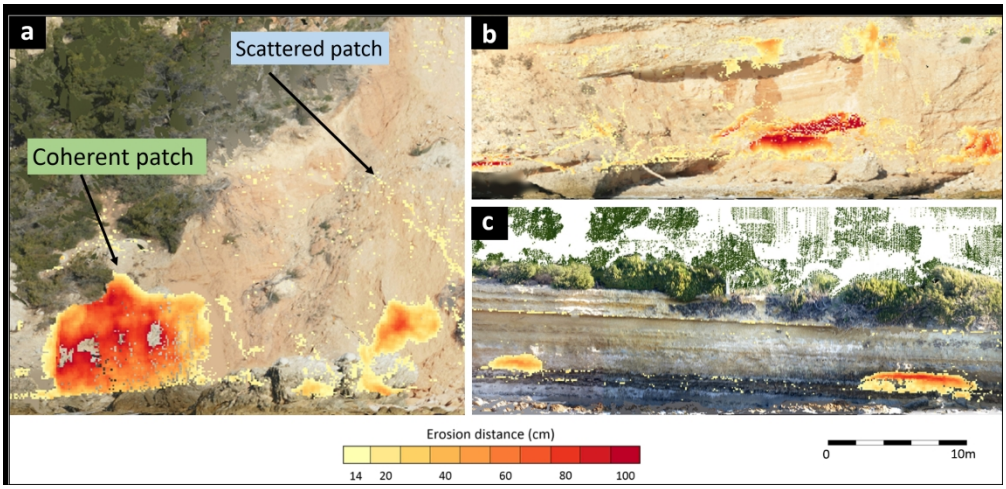


Figure 11. Examples of Digital Surface Model of erosion (DSMe) overlaid on ortho-photography. Erosion scars show up as coherent and scattered patches of absolute distance values.

545x262mm (150 x 150 DPI)

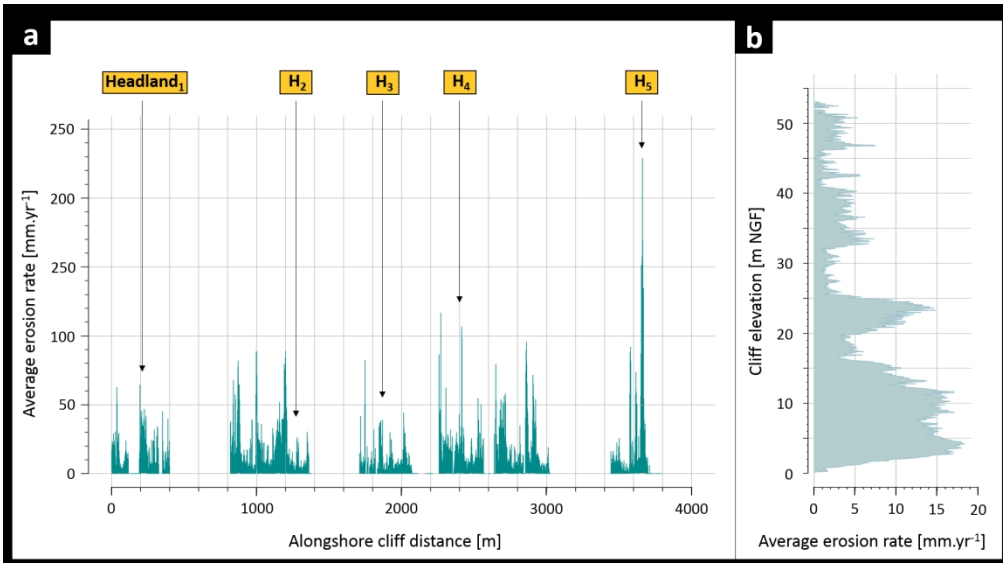


Figure 12. Average erosion rates integrated along-shore (a) and vertically (b). a. All headlands flagged from west to east. The easternmost headland, H5 ("Cap de la Vierge"), locally focused erosion with three large events; b. The vertically integrated profile shows a basal section, up to 15m in height affected by erosion rates above 10mm/year while the upper part of the cliff only reaches 5mm/year.

344x192mm (150 x 150 DPI)

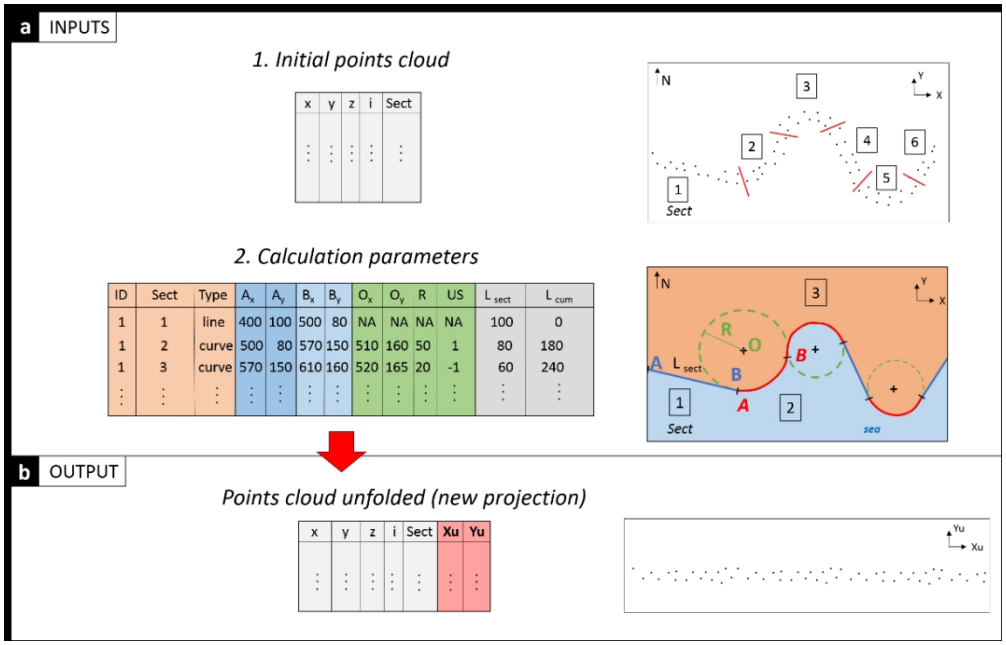


Figure A-1. Concept of unfolding point cloud (inputs and output configuration). a- Processing requires two inputs: 1 Initial point cloud containing the xyzi and sector identifier (Sect) to unfold, 2 Calculation parameters for each sector, whether linear and circular transformation; b- Output is a table which contains initial xyz and new curvilinear continuous coordinates.